SLAC-PUB-14872

Equilibration dynamics and conductivity of warm dense hydrogen

U. Zastrau[a,b], P. Sperling[c], A. Becker[c], T. Bornath[c], R. Bredow[c], T. Döppner[f], S. Dziarzhytski[d], T. Fennel[c], L. B. Fletcher[b], E. Förster[a,e], C. Fortmann[f], S. H. Glenzer[b], S. Göde[c], G. Gregori[g], M. Harmand[d], V. Hilbert[a], D. Hochhaus[j], B. Holst[c], T. Laarmann[d,h], H. J. Lee[b], T. Ma[f], J. P. Mithen[g], R. Mitzner[i], C. D. Murphy[g], M. Nakatsutsumi[k], P. Neumayer[j], A. Przystawik[d], R. Redmer[c], S. Roling[i], M. Schulz[d], B. Siemer[i], S. Skruszewicz[c], J. Tiggesbäumker[c], S. Toleikis[d], T. Tschentscher[k], T. White[g], M. Wöstmann[i], H. Zacharias[i]

[a] *Institut für Optik und Quantenelektronik, Friedrich-Schiller-Universität, Max-Wien-Platz 1, 07743 Jena, Germany*
[b] *SLAC National Accelerator Laboratory, 2575 Sand Hill Road, Menlo Park, CA 94025, USA*
[c] *Institut für Physik, Universität Rostock, D-18051 Rostock, Germany*
[d] *Deutsches Elektronen-Synchrotron DESY, Notkestrasse 85, D-22607 Hamburg, Germany*
[e] *Helmholtz-Institut Jena, Fröbelstieg 3, 07743 Jena, Germany*
[f] *Lawrence Livermore National Laboratory, 7000 East Avenue, Livermore, CA 94550, USA*
[g] *Department of Physics, Clarendon Laboratory, University of Oxford, Parks Road, Oxford, OX1 3PU, UK*
[h] *The Hamburg Centre for Ultrafast Imaging CUI, 22761 Hamburg, Germany*
[i] *Physikalisches Institut, Westfälische Wilhelms-Universität, Wilhelm-Klemm-Str. 10, 48149 Münster, Germany*
[j] *Extreme Matter Institute, GSI Helmholtzzentrum für Schwerionenforschung, 64291 Darmstadt, Germany*
[k] *European XFEL, Albert-Einstein-Ring 19, 22761 Hamburg, Germany*

Abstract

We performed the first experiment on warm dense hydrogen with sub-picosecond time resolution at the XUV free-electron laser facility (FLASH) at DESY (Hamburg). Ultra-fast impulsive electron heating is initiated by a ≤ 300 fs short x-ray burst of 92 eV photon energy. A second pulse probes the sample via x-ray scattering at jitter-free variable time delay. We show that the initial molecular structure dissociates within 0.9 ps, allowing to infer the energy transfer rate between electron and ions. We evaluate Saha and Thomas-Fermi ionization models in the equation of state used in radiation hydrodynamics simulations, predicting plasma parameters that are subsequently used to calculate the static structure factor. Hydrodynamics simulations based on a conductivity model for partially ionized plasma are validated by two-temperature density functional theory coupled to molecular dynamics simulations, and agree with the experimental data. Our results provide important insights and the needed experimental data on transport properties of dense plasmas.

Keywords: x-ray, spectroscopy, laser-matter-interaction, dense plasmas, hydrodynamics, warm dense matter

1. Introduction

The thermodynamic properties of even the simplest element hydrogen remain elusive when it comes to extreme conditions of density, pressure, and temperature. Although not appearing naturally on Earth, hydrogen is found in a diversity of extreme conditions in the solar system and beyond. Knowledge of the equation of state over a broad parameter range is hence critical for modeling stellar and planetary interiors [1], as well as for inertial confinement fusion (ICF) experiments [2].

The mechanisms causing deviation from the ideal gas law have to be taken into account in regions of phase transitions and partial ionization due to electron degeneracy and high density. Microscopic properties of matter related to reflectivity, electrical and thermal conductivity are tied to dynamic energy transport between electrons and ions. On a macroscopic scale, these affect the depth of mixing layers in Jovian planets [3], as well as the formation of a central hot spot and the assembly of a stable thermonuclear fuel layer in ICF implosions [4–6]. Experiments aiming at measuring these quantities hence probe the response of the system to an impulsive pump with high temporal resolution.

Presently, uncertainties in the transport properties in dense matter limit our ability to accurately model such complex systems. Recently, we reported on x-ray measurements in cryogenic hydrogen [7] where ultra-fast electron heating is initiated by a short x-ray burst of duration $\leq$ 300 fs. A second pulse probes the sample via x-ray scattering at variable time delay. It was shown that the initial molecular structure dissociates within 0.9 ps.

In this paper, we show that a proper description of the equilibration dynamics is far from being trivial. We employ different equation of states in radiation-hydrodynamics simulations, and show that our experiment provides a reference point against which ionization models for warm and dense matter states can be validated. Further, we calculate the structure factor for x-ray scattering with different single- and two-temperature approaches, based on the

Email address: ulf.zastrau@uni-jena.de (U. Zastrau)

This material is based upon work supported by the U.S. Department of Energy, Office of Science, Office of Basic Energy Sciences, under Contract No. DE-AC02-76SF00515 and HEP.

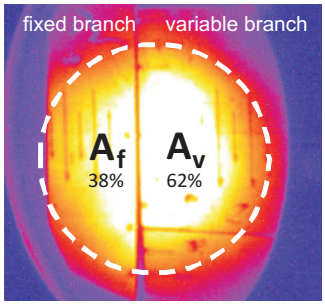

Figure 2: Relative geometrical areas A_f and A_v of the slit-and-delay unit.

plasma temperatures from the hydrodynamics simulations, and validate it against our experimental results.

2. Pump-probe setup

As a versatile diagnostic tool for warm and dense matter states, x-ray scattering was demonstrated on picosecond [8] and nanosecond time scales [9–11]. With the advent of free electron lasers (FELs) the implementation of volumetric x-ray heating [12, 13] and accurate x-ray scattering on the femtosecond time scale is now becoming possible due to the short FEL pulse lengths ($\leq$ 300 fs), their unprecedented peak brightness, and the high repetition rate [14].

To investigate dynamic processes of warm and dense matter on such short time scales, pump-probe experiments are necessary, where a first pulse generates an excited state that is subsequently probed by a second pulse at well-defined time delays. In pioneering experiment [7] we have used the split and delay capability of the **F**ree-electron **LAS**er in **H**amburg (FLASH) [15] (as illustrated in Fig. 1) in order to volumetrically heat liquid hydrogen and subsequently probe it by ultra-fast x-ray scattering.

FLASH has been operated at $E = 92$ eV photon energy with a spectral band width of $\Delta E/E \approx 1.6\%$. An upper limit for the FEL pulse duration of $\leq$ 300 fs is estimated from the measured electron bunch duration ($\sim$ 300 fs FWHM). The bunch charge was 0.33 nC and the bunch energy was $\sim$ 140 μJ at a repetition rate of 10 Hz. The individual x-ray pulse energies have been recorded by a residual gas ionization detector [16], yielding an average initial pulse energy of (200 ± 50) μJ.

The horizontally polarized FEL radiation is geometrically divided by a split-and-delay unit [15, 17]. Likewise a time delay Δt between x-ray pump and probe pulses is introduced with few-fs precision. The intensity ratio of the divided pulses is given by the relative split areas A_f and A_v for the variable and the fixed branch, respectively, multiplied by the transmission of the respective branch. Fig. 2 shows a photograph of the exit port of the split and delay device. The pulses are subsequently focused to a 20×30 μm^2 spot using an elliptical mirror, yielding intensities up to (27 ± 0.6) TW/cm^2 for the variable-delay branch and (19 ± 0.4) TW/cm^2 for the fixed branch. See Tbl.1 for a detailed table showing the of the transmission of the beamline components.

Table 1: FLASH beamline efficiency for 13.5 nm wavelength, accounting for the spit-and-delay unit. GMD - gas monitor detector, VLS - variable line spacing beamline spectrometer.

beamline properties		
GMD	(200 ± 50)	μJ
BL2 [16]	(64 ± 4) μJ	
VLS [16]	$\sin 0.9$	
pulse duration	≤ 300	fs
focal spot area	$6 \cdot 10^{-6}$	cm^2
split and delay		
fixed-delay branch		
relative split area A_f	0.38	
reflectivity [15, 17]	0.75	
total transmission	0.164	
pulse energy	33.5	μJ
power	$1.12 \cdot 10^8$	W
intensity	(19 ± 0.4)	TW/cm^2
variable-delay branch		
relative split area A_v	0.62	
reflectivity [15, 17]	0.67	
total transmission	0.239	
pulse energy	48.8	μJ
power	$1.63 \cdot 10^8$	W
intensity	(27 ± 0.6)	TW/cm^2

The FEL pulses hit a (18 ± 3) μm diameter cryogenic hydrogen jet with mass density of 0.08 g/cm^3 (5×10^{22} cm^{-3}) and temperature of 20 K, prepared in a liquid helium-cooled cryostat [18]. With 60 m/s flow velocity each FLASH pulse scatters from an unperturbed sample. During hydrogen injection the vacuum chamber was at a pressure of 10^{-5} mbar.

3. X-ray heating

We employ 92 eV soft x-ray radiation to be in a regime where the photon energy is well above the plasma frequency for liquid density hydrogen. This leads to a high penetration depth with an absorption length l_{abs}=11 μm [19], comparable to the hydrogen jet radius of $\sim$ 9 μm. The initial energy deposition via photo absorption is not uniform, as FEL intensities of I_0 are present at the target front side, compared to only $\sim$ $0.2I_0$ at the target rear side. But the generated photo-electrons with kinetic energies of 78 eV are capable of impact-ionizing several molecules and atoms within the FEL pulse duration [20]. This leads to further ionization, molecular heating, and expansion, as well as breaking of the covalent H-H bond (dissociation). All these effects lead to an almost homogeneous electron heating throughout the sample.

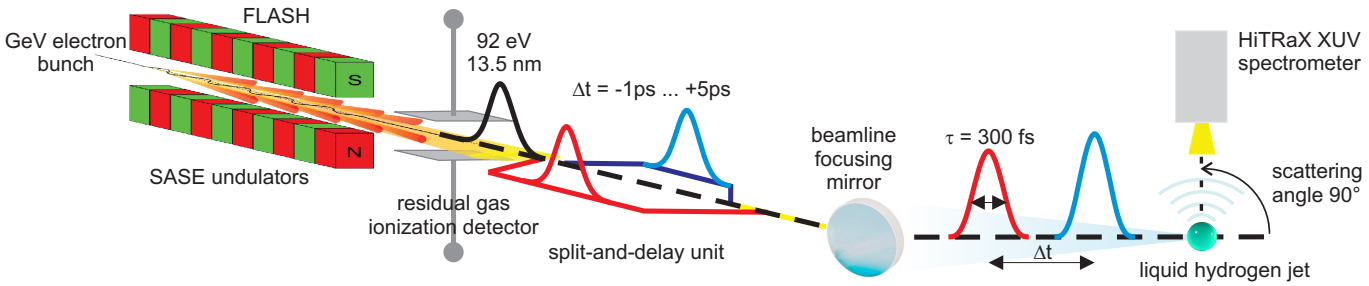

Figure 1: Schematic of the experimental setup [7]. Soft x-ray FEL pulses are split and delayed before they are focused onto a cryogenic hydrogen jet. Scattering is observed with an spectrometer at 90°. For further details refer to the text.

3.1. Radiation hydrodynamics simulations

To describe the temporal variation of the measured scattering intensity, we have performed one-dimensional Lagrangian radiation-hydrodynamic simulations with the code HELIOS [21]. HELIOS solves the equations of motion for a fluid considering the electronic and ionic subsystem as co-moving, while their energies can be handled separately.

Given that the electron-ion equilibration time is an unknown in virtually all high density plasma experiments, we compare the predictions by HELIOS using two different equation of state (EOS) models. PROPACEOS 4.2 calculates the ionization via a Saha model, while PROPACEOS 5.1 uses a Thomas-Fermi model as implemented in the quotidian EOS (QEOS [22]).

The hydrodynamics simulations yield the spatially resolved ion density and the electron and heavy particle temperatures. They were performed for each delay Δt using two 300 fs XUV pulses (the pump pulse at 0 ps and probe at Δt ps), so the pulse duration is accounted for. The plasma conditions are extracted from these simulations at the peak of the probe pulse. In Fig. 3 the average values of the target are shown, because temperature gradients (except for the very surface) are not pronounced. Spatial homogeneity had to be assumed, because it is impossible to perform the subsequent calculations (see sec. 5.1) for inhomogeneous targets with the up-to-date computing capability.

3.2. Ionization

Saha's set of equations yield the ionization degree for a gas at equilibrium temperature T. The single equation for hydrogen gas has an analytic solution. Assuming most of the neutral hydrogen is in the ground state (the statistical weights being $g(H) = 2$ and $g(H^+) = 1$) and charge is conserved, we may write

$$\frac{Z_{\text{free}}^2}{1 - Z_{\text{free}}} = \frac{1}{n}\left(\frac{2\pi m_e kT}{h^2}\right)^{3/2} e^{-13.6\ \text{eV}/kT}. \qquad (1)$$

Since for hydrogen the atomic number $Z = 1$, Z_{free} is both the mean number of free electrons per atom, and the mean ionization degree. The result is plotted in Fig. 4, together with calculations using the program package COMPTRA [23]

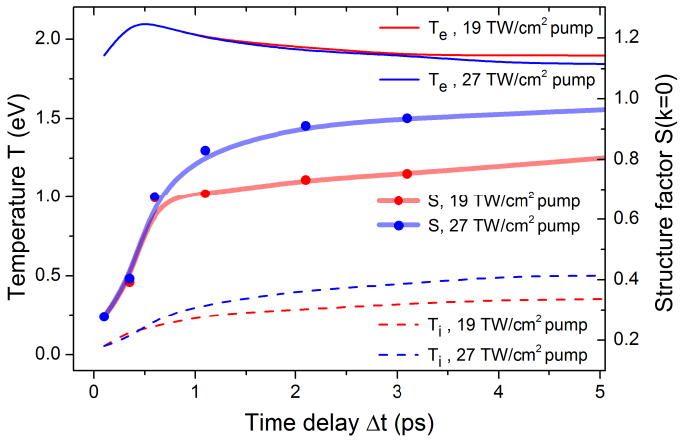

Figure 3: Simulation of the temporal evolution of the plasma parameters and the structure factor. The temperatures of the electronic and atomic-ionic subsystems are calculated using the 1D radiation-hydrodynamics code HELIOS [21]. Also shown is the structure factor at $k = 0$ S. No temporal evolution in the initial ion density is observed. The ionization ranges between 4-6%, temporally following the electron temperature dependency. (Figure taken from [7])

that takes into account higher interaction corrections based on efficient interpolation formulas.

In the two EOS models used for the hydrodynamics simulations, the most striking difference is ionization at low temperatures. Fig. 4 shows the mean ionization Z_{free} of hydrogen at 0.0855 g/cm^3 density for temperatures up to 2 eV. The Saha-like EOS predicts no ionization at T=0 eV, and values $< 10\%$ at $T < 2$ eV. For the ion temperatures of $T_i < 1$ eV relevant in this work, the ionization of the Saha-like EOS is in good agreement with both the results from the analytic solution of eqn. 1 and COMPTRA.

In sharp contrast, the Thomas-Fermi model predicts initially $\sim 50\%$ ionization at T=0 eV. For higher densities the initial ionization further increases (not shown here). Hence QEOS yields pressure ionization for cryogenic hydrogen, which drastically alters energy partitioning between ions and electrons and increases the electron-ion energy transfer rate. Such a metallic state is not observed experimentally, and theoretically predicted only at significantly higher pressures. We conclude that the Thomas-Fermi model is not applicable for small temperatures and low atomic numbers as in our case.

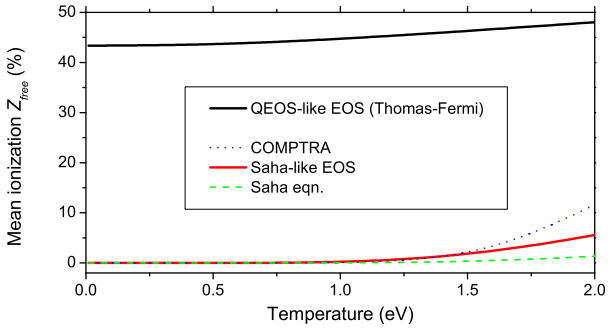

Figure 4: Mean ionization Z_{free} as function of plasma temperature T, comparing Saha- and QEOS-like models for the EOS, as well as the predictions made by the Saha's equation itself and the code COMPTRA [23]. QEOS predicts significant intrinsic pressure ionization, while all other models agree on $< 10\%$ ionization.

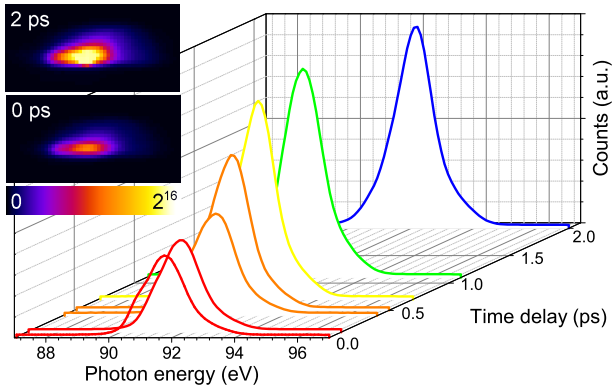

Figure 5: Experimental scattering spectra as function of pump-probe delay, taken from ref. [7]. The inset shows two 16-bit raw spectra, sized 25×50 pixels of $(13.5\ \mu\text{m})^2$ size, with a horizontally oriented spectral axis corresponding to the graph, where the spectral profiles are integrated along the vertical axis.

In order to best fit the scattering data (see sec. 6.1) the simulations have been performed using the Saha-like EOS database PROPACEOS 4.2 [21] that predicts weak ionization between Z_{free} =4-6% (temporally following the electron temperature dependency) and consequently a weak electron-ion energy exchange (of the order of several ps) for the experiment considered in this paper.

4. X-ray probing

At 92 eV photon energy, attenuation via photo absorption has the highest cross section with a small fraction of the incident radiation being also scattered. We use the scattered light of a delayed second pulse to probe the system.

Table 2: Components of the HiTRaX spectrometer and their derived efficiency for 13.5 nm wavelength.

non-dispersive direction		
angular range	4.49	°
collection angle	$78.4 \cdot 10^{-3}$	rad
dispersive direction		
distance source-mirror	255	mm
mirror length	50	mm
grazing angle	7.3	°
effective mirror aperture	6.35	mm
collection angle	$24.9 \cdot 10^{-3}$	rad
total collection solid angle	$1.95 \cdot 10^{-3}$	sterad
transmissions		
toroidal mirror reflectivity	0.78	
grating diffraction efficiency	0.25	
no filter		
total collection efficiency	$18.9 \cdot 10^{-3}$	sterad
CCD camera		
photon energy	92	eV
band gap	2.6	eV/eh
AD conversion	7	eh/count
quantum efficiency	0.42	
counts per photon	$1.5\bar{3}$	
total counts per photon η	$5.9 \cdot 10^{-4}$	sterad

4.1. Experimental scattering spectra

Scattering is collected at 90° relative to the incident FEL radiation in the vertical plane to account for the horizontal polarization of the FEL [24]. To discriminate between the scattered XUV photons and plasma self-emission or energetic particles, we employ the XUV spectrometer HiTRaX [25]. It features a toroidal mirror 255 mm from the target, providing a large solid angle of $1.9 \cdot 10^{-3}$ sr. The spectral dispersion was calibrated in-situ using plasma emission lines [26]. In Tbl. 2 a summary table of the optical elements and their efficiencies is provided.

X-ray scattering spectra are measured for various time delays up to 5 ps. Fig. 5 shows that between 0 ps and 1 ps time delay there is a significant increase of the total scattered intensity. We also notice that the spectral shape shows subtle changes of the wings, mostly dominated by the incident FEL spectrum.

4.2. Thomson scattering

The classical differential light scattering cross section $d\sigma$ per solid angle increment $d\Omega$ of a single electron is given as

$$\frac{d\sigma}{d\Omega} = r_0^2(\epsilon_1 \cdot \epsilon_2)^2, \tag{2}$$

where $r_0 = 2.8210^{-5}$ Å is the classical electron radius and ϵ_1 and ϵ_2 are the polarization vectors of the incoming and outgoing waves. In our case, the incoming x-rays are linearly polarized in the horizontal direction, while the outgoing wave is observed in the vertical direction, thus the

polarization vectors are parallel to each other ($\epsilon_1 \cdot \epsilon_2 = 1$). Hence the number of scattered photons N_{scat} per solid angle $d\Omega$ and per incident photons N_{inc} is given by [27]

$$\frac{1}{N_{inc}} \frac{\mathrm{d}N_{scat}(t)}{\mathrm{d}\Omega} = \frac{V n_i}{A} Z r_0^2 \int \mathrm{d}\omega \, S(k, \omega; t), \qquad (3)$$

where V is the scattering volume, n_i is the heavy particle density (ions and atoms), A is the irradiated area (the focal spot being larger than the sample), $Z = 1$ is the atomic number, r_0 is the classical electron radius, and $S(k, \omega)$ is the structure factor for a momentum transfer k. ω denotes the frequency shift in the case of inelastic scattering.

4.3. Structure factor

From eqn. 3 is it evident that the temporal evolution of the measured x-ray scattering signal is completely characterized by the time-dependent (dynamic) structure factor, $S(k, \omega; t)$. Following Chihara's approach [28, 29], $S(k, \omega)$ can be expressed by a sum of independent contributions:

$$\begin{aligned} S(k,\omega) \; = & \overbrace{Z_{\mathrm{free}} S^0_{ee} \cdot (k,\omega)}^{\text{free electrons}} + \overbrace{|f(k)+q(k)|^2 S_{ii}(k,\omega)}^{\text{bound electrons}} \\ & \underbrace{+ Z_{\mathrm{bound}} \int \mathrm{d}\omega' S_c(k,\omega) S_s(k,\omega-\omega')}_{\text{bound-free transitions (Raman)}} . \end{aligned} \qquad (4)$$

In the first term, $S^0_{ee}(k, \omega)$ describes the scattering off free electrons weighted by Z_{free}, the mean number of free electrons per hydrogen atom. Due to the small ionized fraction of $Z_{\mathrm{free}} < 10$ % the scattering off free electrons can be neglected.

In the second term, $S_{ii}(k, \omega)$ characterizes the scattering off tightly bound electrons - weighted by the atomic form factor $f(k)$ - and weakly bound electrons, weighted by the screening function $q(k)$. In the present case of a hydrogen plasma, we may assume [30]

$$\lim_{k \to 0} |f(k) + q(k)| = Z_{\mathrm{bound}} + Z_{\mathrm{free}} \; = \; Z \; = \; 1. \qquad (5)$$

Hence $|f + q|^2 = 1$ is constant for $k \to 0$ and the signal is only dependent on S_{ii}.

The third term describes Raman-type transitions, where inner shell electrons are excited to the continuum [30, 31] (taken into account via the factor S_c), convoluted with the ion motion S_s. The Raman term is weighted by the mean number of bound electrons per atom Z_{bound}. For 92 eV soft x-rays, the maximum Compton recoil energy transfer of $\hbar\omega = (\hbar k)^2/2m_e = 33$ meV (in a backscatter event) is insufficient to excite bound electrons into the continuum.

At 90° scattering angle, the momentum transfer amounts to $k = \|\mathbf{k_1} - \mathbf{k_2}\| = 0.0348$ $\mathrm{a_B^{-1}}$. Here $\mathbf{k_1}$ and $\mathbf{k_2}$ are the incident and scattered x-ray wave numbers, respectively. For our conditions $kr \ll 1$, where r is the mean inter-particle separation, which means that the probed length $\lambda^* = 2\pi/k$ is much larger than the inter-particle distance, and we probe the collective behavior of a large number of particles. Since this value of k is sufficiently close to zero we use the structure factor at zero momentum transfer, $S(k = 0)$, which is a measure for the sum of all short and long-range electron correlations (see sec. 5.4). The validity of this approach has been verified by hyper-netted chain (HNC) calculations.

On the other hand, $kD \gg 1$, where D is the hydrogen jet diameter. With geometrically finite objects more photons are scattered from the interfaces (the jet surface). The underlying physics is in first order similar to volumetric scattering, including its temporal dependence.

5. Calculating structural properties

Hydrodynamics simulations provide the thermodynamic, macroscopic properties of a statistical system. But in order to calculate the structure factor, which dictates the experimentally observed scattering via eqn. 3, knowledge of the microscopic structure of the hydrogen plasma is essential.

5.1. Density functional theory

The simulated particle density and the temperatures of electrons and ions/atoms from HELIOS are used as input parameters for ab-initio two-temperature density-functional-theory molecular dynamics (2T-DFT-MD) simulations [32]. The code uses the physical picture, which considers only electrons and nuclei and all other features (such as long-lived bound states, atoms, and molecules) are correlations. The use of two-temperature DFT is a novel method [33] taking into account all equilibrium correlations, except the missing change of the wave functions imposed by non-equilibrium dynamics/relaxation. It treats all electrons for given arbitrary positions of the nuclei r. From the resulting electric fields E(r) the Coulomb forces on the nuclei are derived and move these in the molecular dynamics (MD) step.

For the 2T-DFT-MD we use the Vienna Ab-initio Simulation Package (VASP) [34]. DFT at finite temperatures is implemented in VASP solving the Kohn-Sham equations self-consistently to minimize the free energy $F[n(\mathbf{r})]$ of the system as a functional of the local electron density

$$n(\mathbf{r}) = \sum_{i=1}^{N} f(\epsilon_i, T) |\phi_i(\mathbf{r})|^2,$$

where the wave functions are weighted with the Fermi distribution $f(\epsilon_i, T)$. The effective potential defining all interactions in the system includes ion-background contributions $v_{\mathrm{ext}}(\mathbf{r})$, the Hartree energy, and the exchange-correlation functional $F_{XC}[n(\mathbf{r})]$. The heavy particle temperature T_i is controlled with a Nosé thermostat [35] while the electron temperature T_e is defined via the Fermi-weighting of the electron distribution. Convergence is checked with respect to the particle number, the **k**-point sets used for the evaluation of the Brillouin zone, and the energy cut-off for the plane wave basis set. The Coulomb interactions

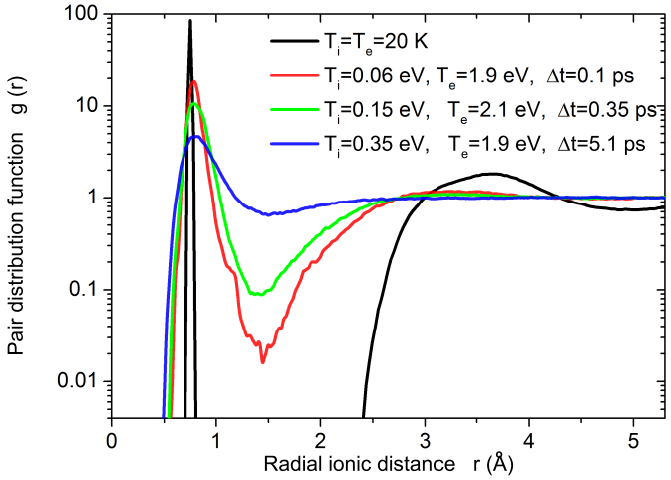

Figure 6: Calculated pair distribution function, from ref. [7]. Shown is the pair distribution function $g(r)$ as function of the radial interparticle distance r for different time delays and temperatures. For cryogenic hydrogen (T=20 K), a peak at $r \sim 0.75$ Å indicates the distance in the H_2 molecule. With increasing temperature the molecular bonds break and the intensity of the peak drops.

between the electrons and ions are treated using projector-augmented wave potentials [36] with a converged energy cutoff of 1400 eV. We chose 64 atoms, the Baldereschi mean value point [37] and use the exchange-correlation functional of **P**erdew, **B**urke, and **E**rnzerhof (PBE) [38] which has been shown to give reasonable results for warm dense matter states [32, 39]. The DFT signal follows the rise of the ion temperature, therefore the energy transfer from electrons to ions and atoms is important.

The ionization degree from HELIOS is not used as an input for DFT, but is derived independently based on the plasma temperatures, pressure, and impact ionization. For the estimation of the collision frequency for electrons and atoms the rigid sphere model is used which assumes elastic impact.

5.2. Pair distribution function g(r)

DFT provides the radial pair distribution function $g(r)$ of atoms and ions. Fig. 6 shows $g(r)$ for different temperatures, corresponding to different time delays. A pronounced peak in the distribution function is seen at radius $r \sim 0.75$ Å which coincides with the distance of the molecular atom pair [32] and characterizes an undissociated molecular system. With increasing temperature the molecular peak drops and broadens and a continuous distance distribution arises, corresponding to bond breakage and plasma formation. Fig. 7 illustrates the respective positions of hydrogen atoms, according to $g(r)$. Hence, an ideal plasma state is reached if the pair distribution function is unity, e.g. all particles are randomly distributed.

5.3. Dissociation of molecules

The hydrogen molecule has a strong covalent bond with a binding energy of $E_{\mathrm{H-H}} = 4.52$ eV. In the DFT simulations, this binding energy is accounted for by solving

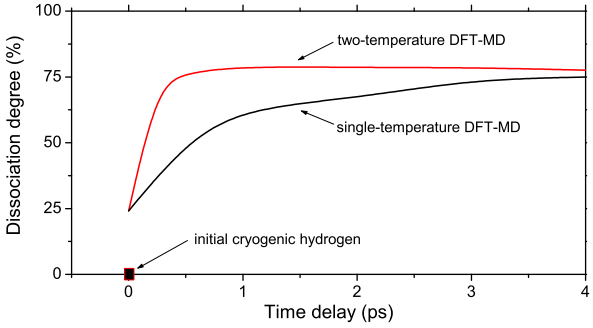

Figure 8: Dissociation degree of hydrogen molecules as function of delay for 2T-DFT ($T_e \neq T_i$) and 1T-DFT ($T_e \equiv T_i$).

Schroedinger's equation. If no FEL is applied, the system stays at cryogenic temperatures and therefore remains completely molecular (left panel in Fig. 7). When the FEL is applied, bond breaking occurs due to the elevated electron and ion temperatures, derived from HELIOS simulations. These temperatures obey a Maxwell-Boltzmann distribution, so that even at low temperatures a fraction of particles carry significant kinetic energy. In an electronic system with $T_e = 2$ eV a considerable number of electrons have energies exceeding the molecular bond energy $E_{\mathrm{H-H}}$. This also applies for the ionic subsystem with temperatures $T_i \leq 1$ eV. Fig. 8 shows the dissociation degree for 2T-DFT ($T_e \neq T_i$) and 1T-DFT ($T_e \equiv T_i$) for comparison as function of delay time. Clearly, in the two-temperature simulations the dissociation degree is higher due to the initially hotter electron system, which efficiently dissociate molecules via impact ionization. Evidently the temporal evolution of the correlations is strongly dependent on the energy partition between electrons and protons, requiring a two-temperature approach.

5.4. Deriving S(k) from g(r)

In general, the structure factor $S(k)$ is related to the pair distributions $g(r)$ by [40]

$$S(k) = \underbrace{1}_{\text{ideal system}} + \underbrace{n_i \int (g(r)-1) e^{\mathrm{i}\vec{k}\cdot\vec{r}} \mathrm{d}\vec{r}}_{\text{correlations}}. \qquad (6)$$

Eqn. 6 is composed of a constant contribution of an ideal system ($S \equiv 1$) and the correlations, given by a Fourier transform of the total correlation function $(g(r) - 1)$.

For zero momentum transfer, $k = 0$, this Fourier transform switches to a integration over the total correlation functions:

$$S(0) = 1 + n_i \int \mathrm{d}\vec{r}\,(g(r) - 1). \qquad (7)$$

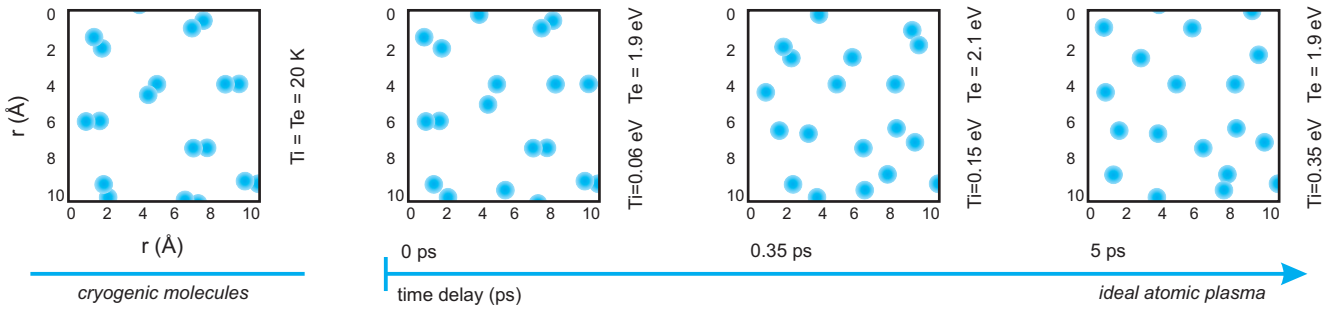

Figure 7: Two-dimensional illustration of the hydrogen atoms. Shown is the transition from initial cryogenic hydrogen (left) to an atomic ideal plasma (right).

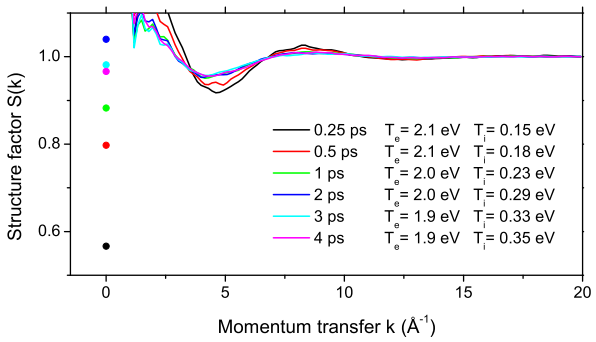

Figure 9: Shown is the calculated structure factor $S(k)$ for different time delays, extracted from the DFT simulations. For $k < 1.25$ Å the DFT simulations are not trustable, but for $k = 0$ (points) they are valid.

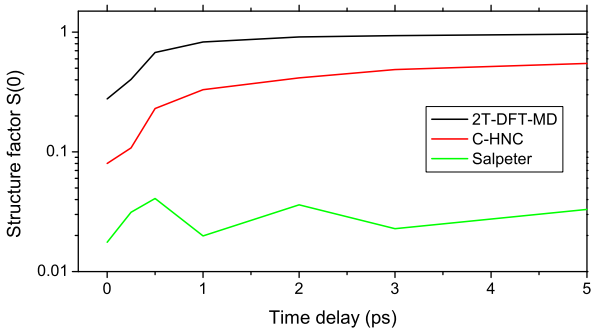

Figure 10: Structure factor $S(k = 0)$ calculated with 2T-DFT-MD, with C-HNC, and in Salpeter approximation.

Therefore the correlations for all distances r between the particles become relevant for $S(0)$.

In Fig. 9 the structure factor $S(k)$ for different time delays extracted from the DFT simulations are shown. We see that for larger momentum transfer (e.g., higher photon energy and/or backscatter geometry) the structure factor gets less sensitive to the particle correlations. Highest sensitivity is achieved for $k = 0$ as realized in this work.

For $k < 1.25$Å the DFT simulations are not valid due to the limited size of the simulation box, but for $k = 0$ they are valid, since $S(0)$ reduces to the ratio between the real (κ_T) and the ideal (κ_T^{id}) isothermal compressibilities:

$$S(0) = \frac{\kappa_T}{\kappa_T^{\mathrm{id}}}, \tag{8}$$

The ideal compressibility is simply given by $\kappa_T^{\mathrm{id}} = 1/(n_i k_B T)$, while the real compressibility is obtained from the equation of state via $\kappa_T = (\partial\rho/\partial p)/\rho$. This means that $S(0)$ is derived from the density change as function of pressure. The compressibility can only be related to the total correlations for $r \to$ inf.

The predicted time dependence of $S(0)$ is shown in Fig. 3. At initial times, we see that $S(0)$ differs from unity indicating a highly correlated system. At later times, $S(0)$ approaches 1 which can be explained by a transition from molecular liquid hydrogen to an almost uncorrelated fluid-like structure (cf eqn. 7). When comparing the $S(0)$ inferred from DFT to the ion temperature shown in Fig. 3, S does not change very much once T_i exceeds 0.25 eV, since beyond this point the majority of the molecular bonds are broken (see also Fig. 8).

5.5. Alternative approaches to calculate S(0)

Fig. 10 shows a comparison of the results for $S(0)$ calculated with 2T-DFT, with the Classical-map Hyper-Netted-Chain (C-HNC) approach, and in Salpeter approximation [41]. Note the logarithmic ordinate. As compared to 2T-DFT-MD, the Salpeter approximation predicts a structure factor that is both undersized and misshaped, but the results of C-HNC are qualitatively similar to DFT. Since C-HNC simulations take considerably less computational time as compared to DFT, they are suitable for fast predictions.

6. Results

6.1. Experimental data

In Fig. 11 the scattered fraction of the photons is plotted versus time delay. The data was normalized to the

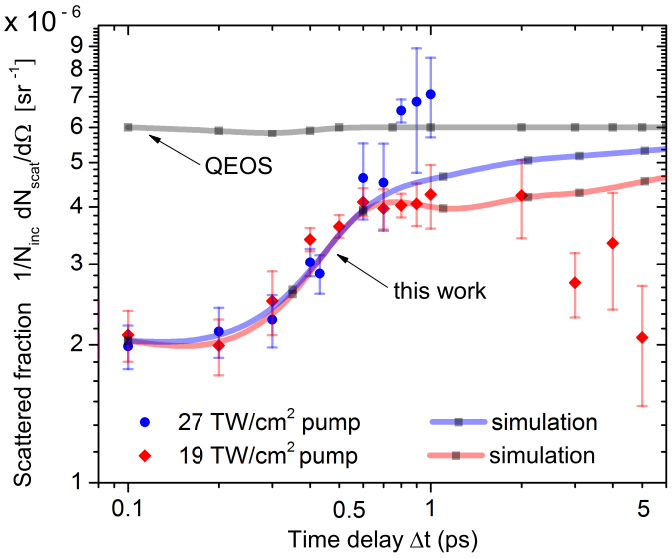

Figure 11: Temporal evolution of the measured and simulated x-ray scattering. A total of 300 exposures were grouped together by delay, and their errors resemble their root mean square deviations. For the blue data points, ranging from $\Delta t = 0$ ps to 1 ps only, the more intense 27 TW/cm^2 pulse pumps the target, while it is probed by the 19 TW/cm^2 pulse. The red data points, ranging from 0 ps to 5 ps, resemble the inverse case where the pump was less intense (19 TW/cm^2) than the probe (27 TW/cm^2). In both cases, the signal increases within 1 ps, and for the more intense pump the amplitude is larger.

incoming photon number N_{inc} (see Tbl. 1) and the XUV spectrometer efficiency η (see Tbl.2), calculated from the specifications.

We observe a significant increase of the signal for times ≤ 1 ps. Stronger pumping of the liquid hydrogen (corresponding to 27 TW/cm^2) leads to more scatter, because the particles are less ordered. For the weaker pump (19 TW/cm^2), we were also able to measure time delays up to 5 ps. First we observe that after 1 ps the scattering amplitude stops growing, flattens until about 2 ps and slowly decreases at 5 ps. This decrease could be attributed to recombination processes in weakly ionized hydrogen not currently implemented in our hydrodynamic calculations. Best agreement with the simulations (as shown in Fig. 11) is achieved when multiplying the measured values with a factor of 2.6, which could be attributed to surface-enhanced scattering as discussed in sec. 4.3.

A Gaussian fit to the experimental data yields a valley-to-peak time of (1.1 ± 0.2) ps. After deconvolution of the probe pulse duration, we derive that cryogenic molecular hydrogen responds to an impulsive heating of the electrons within ~ 0.9 ps.

6.2. Equilibration time and conductivity

The hydrodynamics simulations employ the classical Spitzer equilibration time

$$\tau = \frac{32\sqrt{2}\pi\epsilon_0^2 m_i}{\sqrt{m_e}e^4} \frac{1}{Z_{\text{free}}^2 n_i \ln\Lambda} (k_B T_e)^{3/2} \qquad (9)$$

with $\ln\Lambda$ being the Coulomb logarithm. Using the classic expression, the latter becomes negative for degenerate plasmas, e.g. at low temperatures and high densities, which is unphysical. To overcome this limitation, improved expressions for $\ln\Lambda$ have been proposed [42, 43], yielding $1 \leq \Lambda \leq 8$ for our conditions. For a partially ionized plasma, a sub-plasma is considered: $n_i \rightarrow Z_{\text{free}} n_h$, where n_h is the density of heavy particles. Fig. 11 shows that the hydrodynamics simulations using the Saha-like EOS and the Spitzer model are in good agreement with the measured temporal evolution of the scattering amplitude.

We further prove that a Saha ionization model as implemented in this work is superior to the Thomas-Fermi model as implemented in QEOS [22]. The latter predicts about order of magnitude too short equilibration times, generating a plasma with $S(0) \sim 1$ well within the FEL pulse duration. Hence no pump-probe delay dependence for $S(0)$ is predicted using QEOS (see Fig. 11).

It is not self-evident that the equilibration time derived from hydrodynamic simulations agrees with the DFT-MD results, because the Spitzer model (eqn. 9) is not explicitly implemented in the latter. Since our DFT simulations provide the electrical conductivity, the mean electron-ion collision time can be derived from a Drude fit at fixed time delay [44]. This approach is valid because the hydrogen plasma exhibits metallic properties, obeying the Drude theory. Hence no temporal resolution is needed to infer the collision time.

The ac conductivity $\sigma(\omega)$ for frequency ω is described by the Drude model by [45]

$$\sigma(\omega) = \frac{\sigma(\omega = 0)}{1 + (\omega\tau_c)^2} \ .$$

where τ_c is the collision time. Fig. 12 shows the results derived from DFT-MD as function of delay time. The mean ionization degree Z_{free} and the plasma conductivity σ (after PBE, see sec. 5.1) follow the temporal evolution of T_e (left axis). The equilibration times τ range between $(0.65 \leq \tau \leq 0.81)$ ps (scaling as $1/Z_{\text{free}}$), in good agreement with our measured value of 0.9 ps. Heating of the atoms and ions takes of order $m_p/(2m_e) \sim 10^3$ longer than the time between individual electron-ion collisions, because it takes many collisions - in particular if electrons collide with protons.

6.3. Consistency of ionization models

With the static electrical conductivity from the DFT data at $\omega = 0$, also the free electron density n_e can be calculated via

$$\sigma(\omega = 0) \equiv \sigma_0 = \frac{n_e e^2 \tau}{m_e}$$

where m_e is the electron mass. As shown in Fig. 12, the DFT fit leads to an ionization degree of 4.5 to 6.5% [45], which is again consistent with ionization using the Saha-like EOS, yielding values between 4 and 6%.

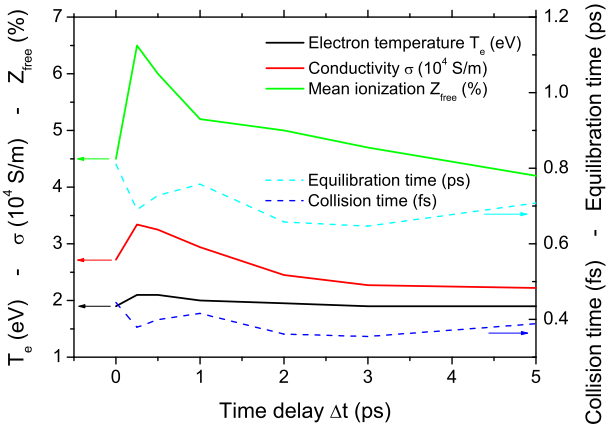

Figure 12: Temporal evolution of the plasma parameters derived from DFT-MD. The electron temperature T_e is an input parameter from HELIOS. The ionization degree Z_{free} and the plasma conductivity σ follow the temporal evolution of T_e (left axis). On the right axis, the collision and equilibration times are plotted.

7. Conclusion and Outlook

We studied hydrogen plasma with ion temperature $T_i \leq 1$ eV and 0.08 g/cm^3 solid density. These conditions do not catch the laboratory equivalent of ICF plasmas or Jovian planet interiors, but nevertheless allows inferring transport properties such as electron heating, equilibration dynamics, and plasma conductivity.

We show that driving hydrogen from initially cryogenic condensed matter to an ideal plasma poses several challenges to the employed models. We evaluated ionization models for the equation of state data, and show that a Saha-like model is superior to a Thomas-Fermi approach as implemented in QEOS. QEOS predicts an initially metallic state with $\sim 40\%$ ionization, in conflict with experimental data. In principle it accounts for degenerate plasmas, important in the framework of warm and dense matter, but is not accurate for the low temperatures and low atomic numbers found in astrophysically relevant plasmas, dealt with in this work.

In this regime, also the concept of the Coulomb logarithm $\ln\Lambda$ breaks down. It needs to be expressed by alternative approaches as it enters the hydrodynamic simulations via the Spitzer conductivity model. We shown that values of $1 \leq \Lambda \leq 8$ yield equilibration times τ consistent with both measurements and DFT-MD results.

Finally, an independent treatment of electron and ion temperatures in DFT-MD is shown to be necessary for accurate ab-initio calculations of the microscopic properties such as dissociation, and hence the structure factor.

Numerical simulations indicate that the Rayleigh-Taylor growth is highly sensitive to thermal conduction [46]. Reduction in the heat diffusion coefficient by a factor 10 corresponds to an increase by a factor $\sim$2 in the mixing layer between compressed DT and beryllium in ICF capsules. In the same way, this is also expected to change the predicted depth of mixing layers in Jovian planets [3, 6]. Hence, our results provide important insights and needed experimental data on transport effects which will shed light on the detailed understanding of dense plasmas.

8. Acknowledgments

The authors thank the FLASH machine and experiments team for their great support. The assistance of the Bundesministerium für Bildung und Forschung within the priority research area FSP 301 FLASH, the Deutsche Forschungsgemeinschaft within the SFB 652, CUI, and the VolkswagenStiftung is acknowledged. Partial funding from UK EPSRC grant EP/G007187/1 and from the French Agence Nationale de la Recherche under Grant IRONFEL - ANR-12-PDOC-0011. This work was partially performed under the auspices of the U.S. Department of Energy by Lawrence Livermore National Laboratory under Contract No. DE-AC52-07NA27344 and was supported by LDRD 11-ERD-050. This work was partially supported by DOE Office of Basic Energy Sciences, Materials Sciences and Engineering Division, under Contract DE-AC02-76SF00515. The DFT-MD simulations were performed at the North-German Supercomputing Alliance (HLRN). Supporting simulations were performed at the John von Neumann-Institut for computing.

References

[1] N. Nettelmann, et al., Ab initio equation of state data for hydrogen, helium, and water and the internal structure of Jupiter, Astrophys. J. 683 (2008) 1217–1228.
[2] J. Lindl, et al., The physics basis for ignition using indirect-drive targets in the National Ignition Facility, Phys. Plasmas 11 (2004) 339–491.
[3] J. Leconte, G. Chabrier, A new vision of giant planet interiors: Impact of double diffusive convection, A&A 540.
[4] A. J. Mackinnon, J. L. Kline, et al., Assembly of high-areal-density deuterium-tritium fuel from indirectly driven cryogenic implosions, Phys. Rev. Lett. 108 (2012) 215005–215009. doi:10.1103/PhysRevLett.108.215005.
[5] S. Glenzer, D. Callahan, A. MacKinnon, J. Kline, G. Grim, E. Alger, R. Berger, L. Bernstein, R. Betti, D. Bleuel, et al., Cryogenic thermonuclear fuel implosions on the national ignition facility, Physics of Plasmas 19 (2012) 056318–056332.
[6] S. P. Regan, et al., Hot-spot mix in ignition-scale implosions on the NIF, Phys. Plasmas 19 (2012) 056307–056313.
[7] U. Zastrau, P. Sperling, M. Harmand, et al., Resolving ultrafast heating of dense cryogenic hydrogen, Phys. Rev. Lett. 00 (0) (2007) 00000.
[8] A. Kritcher, et al., Ultrafast x-ray Thomson scattering of shock-compressed matter, Science 322 (2008) 69–71.
[9] S. H. Glenzer, et al., Observations of plasmons in warm dense matter, Phys. Rev. Lett. 98 (2007) 065002–065005.
[10] G. Gregori, et al., X-ray measurements of radiative heating and cooling dynamics, Phys. Rev. Lett. 101 (2008) 045003–045006.
[11] E. G. Saiz, G. Gregori, D. O. Gericke, J. Vorberger, B. Barbrel, R. Clarke, R. R. Freeman, S. Glenzer, F. Khattak, M. Koenig, et al., Probing warm dense lithium by inelastic x-ray scattering, Nat. Phys. 4 (12) (2008) 940–944.
[12] B. Nagler, U. Zastrau, R. R. Fäustlin, S. M. Vinko, T. Whitcher, A. Nelson, R. Sobierajski, J. Krzywinski, J. Chalupsky,

E. Abreu, et al., Turning solid aluminium transparent by intense soft x-ray photoionization, Nat. Phys. 5 (9) (2009) 693–696.
[13] S. Vinko, O. Ciricosta, B. Cho, K. Engelhorn, H.-K. Chung, C. Brown, T. Burian, J. Chalupskỳ, R. Falcone, C. Graves, et al., Creation and diagnosis of a solid-density plasma with an x-ray free-electron laser, Nature 482 (7383) (2012) 59–62.
[14] W. Ackermann, et al., Operation of a free-electron laser from the extreme ultraviolet to the water window, Nat. Phot. 1 (2007) 336–342.
[15] M. Wöstmann, R. Mitzner, T. Noll, S. Roling, B. Siemer, F. Siewert, S. Eppenhoff, F. Wahlert, H. Zacharias, The xuv split-and-delay unit at beamline bl2 at flash, Journal of Physics B: Atomic, Molecular and Optical Physics 46 (16) (2013) 164005 –.
[16] K. Tiedtke, A. Azima, et al., The soft x-ray free-electron laser FLASH at DESY: beamlines, diagnostics and end-stations, New Journal of Physics 11 (2) (2009) 023029–+.
[17] R. Mitzner, et al., Direct autocorrelation of soft-x-ray free-electron-laser pulses by time-resolved two-photon double ionization of he, Phys. Rev. A 80 (2) (2009) 025402.
[18] S. Toleikis, R. Fäustlin, et al., Soft x-ray scattering using fel radiation for probing near-solid density plasmas at few electron volt temperatures, High Energy Density Physics 6 (1) (2010) 15–20.
[19] P. Sperling, et al., Two-color Thomson scattering at FLASH, High Energy Dens. Phys. 7 (2011) 145149.
[20] R. R. Fäustlin, T. Bornath, T. Döppner, S. Düsterer, E. Förster, C. Fortmann, S. Glenzer, S. Göde, G. Gregori, R. Irsig, et al., Observation of ultrafast nonequilibrium collective dynamics in warm dense hydrogen, Phys. Rev. Lett. 104 (12) (2010) 125002.
[21] J. MacFarlane, I. Golovkin, P. Woodruff, HELIOS-CR – a 1-D radiation-magnetohydrodynamics code with inline atomic kinetics modeling, J. Quant. Spectrosc. Radiat. Transfer 99 (1) (2006) 381–397.
[22] R. M. More, K. H. Warren, D. A. Young, G. B. Zimmerman, A new quotidian equation of state (qeos) for hot dense matter, Physics of Fluids (1958-1988) 31 (10) (1988) 3059–3078. doi:http://dx.doi.org/10.1063/1.866963.
[23] S. Kuhlbrodt, B. Holst, R. Redmer, Comptra04–a program package to calculate composition and transport coefficients in dense plasmas, Contributions to Plasma Physics 45 (2) (2005) 73–88.
[24] A. Höll, T. Bornath, et al., Thomson scattering from near-solid density plasmas using soft x-ray free electron lasers, High Energy Density Physics 3 (1) (2007) 120–130.
[25] R. R. Fäustlin, U. Zastrau, S. Toleikis, I. Uschmann, E. Förster, T. Tschentscher, A compact soft x-ray spectrograph combining high efficiency and resolution, J. Inst. 5 (02) (2010) P02004.
[26] U. Zastrau, et al., In-situ determination of dispersion and resolving power in simultaneous multiple-angle XUV spectroscopy, J. Inst. 6 (10) (2011) P10001–10.
[27] S. H. Glenzer, R. Redmer, X-ray Thomson scattering in high energy density plasmas, Rev. Mod. Phys. 81 (2009) 1625–1663.
[28] J. Chihara, Difference in x-ray scattering between metallic and non-metallic liquids due to conduction electrons, J. Phys. F 17 (1987) 295.
[29] J. Chihara, Interaction of photons with plasmas and liquid metals - photoabsorption and scattering, J. Phys. Cond. Matter 12 (2000) 231.
[30] G. Gregori, S. H. Glenzer, et al., Electronic structure measurements of dense plasmas, Phys. Plasmas 11 (2004) 2754.
[31] S. Sahoo, G. F. Gribakin, G. S. Naz, J. Kohanoff, D. Riley, Compton scatter profiles for warm dense matter, Phys. Rev. E 77 (2008) 046402.
[32] B. Holst, R. Redmer, M. P. Desjarlais, Thermophysical properties of warm dense hydrogen using quantum molecular dynamics simulations, Phys. Rev. B 77 (2008) 184201–184207.
[33] Z. Chen, B. Holst, S. Kirkwood, V. Sametoglu, M. Reid, Y. Tsui, V. Recoules, A. Ng, Evolution of ac conductivity in nonequilibrium warm dense gold, Phys. Rev. Lett. 110 (13) (2013) 135001–135005.
[34] G. Kresse, J. Furthmüller, Efficient iterative schemes for ab initio total-energy calculations using a plane-wave basis set, Phys. Rev. B 54 (1996) 11169 – 11186.
[35] S. Nosé, A unified formulation of the constant temperature molecular dynamics methods, J. Chem. Phys. 81 (1984) 511–519.
[36] P. E. Blöchl, Projector augmented-wave method, Physical Review B 50 (24) (1994) 17953.
[37] A. Baldereschi, Mean-value point in the Brillouin zone, Phys. Rev. B 7 (12) (1973) 5212 – 5215.
[38] J. P. Perdew, K. Burke, M. Ernzerhof, Generalized gradient approximation made simple, Phys. Rev. Lett. 77 (18) (1996) 3865 – 3868.
[39] W. Lorenzen, B. Holst, R. Redmer, First-order liquid-liquid phase transition in dense hydrogen, Phys. Rev. B 82 (19) (2010) 195107–195112.
[40] M. Shimoji, Liquid metals: an introduction to the physics and chemistry of metals in the liquid state, Vol. 266, Academic Press London, 1977.
[41] D. Evans, J. Katzenstein, Laser light scattering in laboratory plasmas, Reports on Progress in Physics 32 (1) (1969) 207.
[42] M. R. Zaghloul, M. A. Bourham, J. M. Doster, Energy-averaged electron–ion momentum transport cross section in the born approximation and debye–hückel potential: Comparison with the cut-off theory, Physics Letters A 268 (4) (2000) 375–381.
[43] D. Gericke, M. Murillo, M. Schlanges, Dense plasma temperature equilibration in the binary collision approximation, Phys. Rev. E 65 (3) (2002) 036418 – 036422.
[44] K. U. Plagemann, P. Sperling, R. Thiele, M. Desjarlais, C. Fortmann, T. Döppner, H. Lee, S. Glenzer, R. Redmer, Dynamic structure factor in warm dense beryllium, New J. Phys. 14 (5) (2012) 055020.
[45] P. Renaudin, V. Recoules, P. Noiret, J. Clérouin, Electronic structure and equation of state data of warm dense gold, Physical Review. E, Statistical Physics, Plasmas, Fluids, and Related Interdisciplinary Topics 73 (5).
[46] B. Hammel, S. Haan, D. Clark, M. Edwards, S. Langer, M. Marinak, M. Patel, J. Salmonson, H. Scott, High-mode Rayleigh-Taylor growth in NIF ignition capsules, High Energy Dens. Phys. 6 (2) (2010) 171–178. doi:http://dx.doi.org/10.1016/j.hedp.2009.12.005.